Supporting Information

Polaritonic probe of an emergent 2D dipole interface

Daniel J. Rizzo[1,†,*], Jin Zhang[2,†], Bjarke S. Jessen[1], Francesco L. Ruta[1,3], Matthew Cothrine[4], Jiaqiang Yan[4,5], David G. Mandrus[4,5], Stephen E. Nagler[6,7], Takashi Taniguchi[8], Kenji Watanabe[9], Michael M. Fogler[10], Abhay N. Pasupathy[1], Andrew J. Millis,[1,11] Angel Rubio[2,11,12,*], James C. Hone[13], Cory R. Dean[1,*], D.N. Basov[1,*]

[1]Department of Physics, Columbia University, New York, NY, 10027, USA

[2]Theory Department, Max Planck Institute for Structure and Dynamics of Matter and Center for Free-Electron Laser Science, 22761 Hamburg, Germany

[3]Department of Applied Physics and Applied Mathematics, Columbia University, New York, NY, 10027, USA

[4]Department of Materials Science and Engineering, University of Tennessee, Knoxville, Tennessee 37996, USA

[5]Materials Science and Technology Division, Oak Ridge National Laboratory, Oak Ridge, Tennessee 37831, USA

[6]Neutron Scattering Division, Oak Ridge 431 National Laboratory, Oak Ridge, Tennessee 37831, USA

[7]Department of Physics and Astronomy, University of Tennessee, Knoxville, Tennessee 37996, USA

[8]Research Center for Materials Nanoarchitectonics, National Institute for Materials Science, 1-1 Namiki, Tsukuba 305-0044, Japan

[9]Research Center for Electronic and Optical Materials, National Institute for Materials Science, 1-1 Namiki, Tsukuba 305-0044, Japan

[10]Department of Physics, University of California San Diego, La Jolla, California 92093, United States

[11]Center for Computational Quantum Physics, Flatiron Institute, New York, New York 10010, USA

[12]Nano-Bio Spectroscopy Group, Universidad del País Vasco UPV/EHU, San Sebastián 20018, Spain

[13]Department of Mechanical Engineering, Columbia University, New York, NY, 10027, USA

[†]D.J.R. and J.Z. contributed equally to this paper

*Correspondence to: db3056@columbia.edu, cd2478@columbia.edu, angel.rubio@mpsd.mpg.de, and djr2181@columbia.edu

Table of Contents:

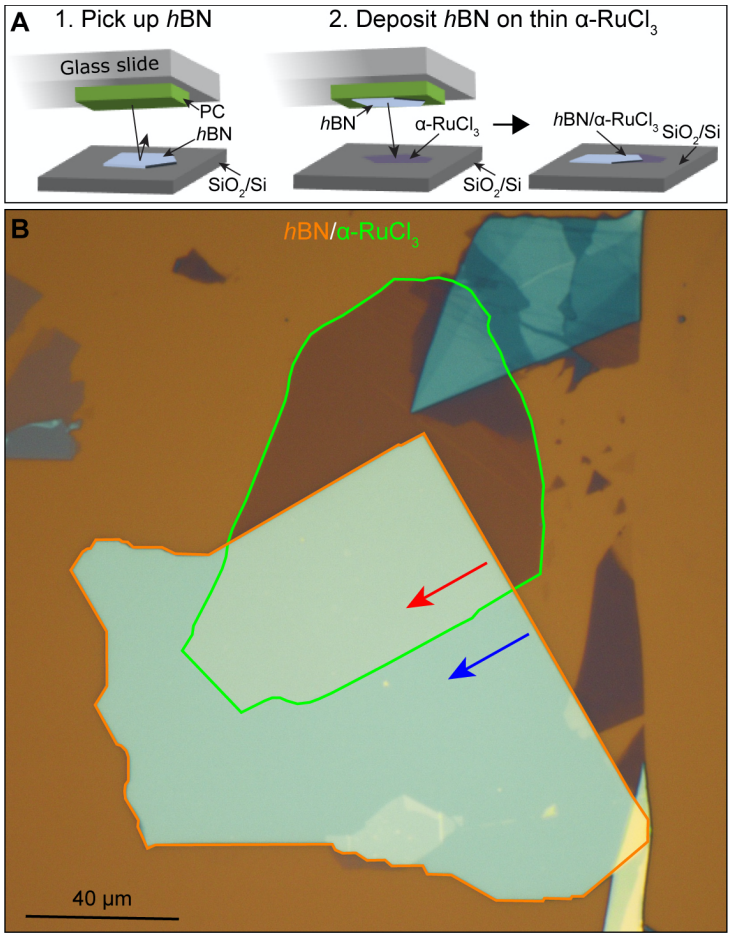

Figure S1. *h*BN/α-$RuCl_3$ device fabrication. (**A**) Diagram of two steps for *h*BN/α-$RuCl_3$ device assembly. In the first step, a PC-coated glass slide is used to pick up an exfoliated crystal of 22-nm-thick thick *h*BN on an SiO_2/Si substrate. In the second step, the *h*BN is deposited onto an exfoliated flake of few-layer α-$RuCl_3$. The final structure was constructed such that part of the *h*BN is directly on SiO_2 and part is on top of the α-$RuCl_3$. (**B**) Optical image of *h*BN/α-$RuCl_3$ device with the *h*BN outlined in orange and the α-$RuCl_3$ outlined in green. The red and blue arrows indicate the position of nano-optical imaging of PhPs on and off the α-$RuCl_3$, respectively.

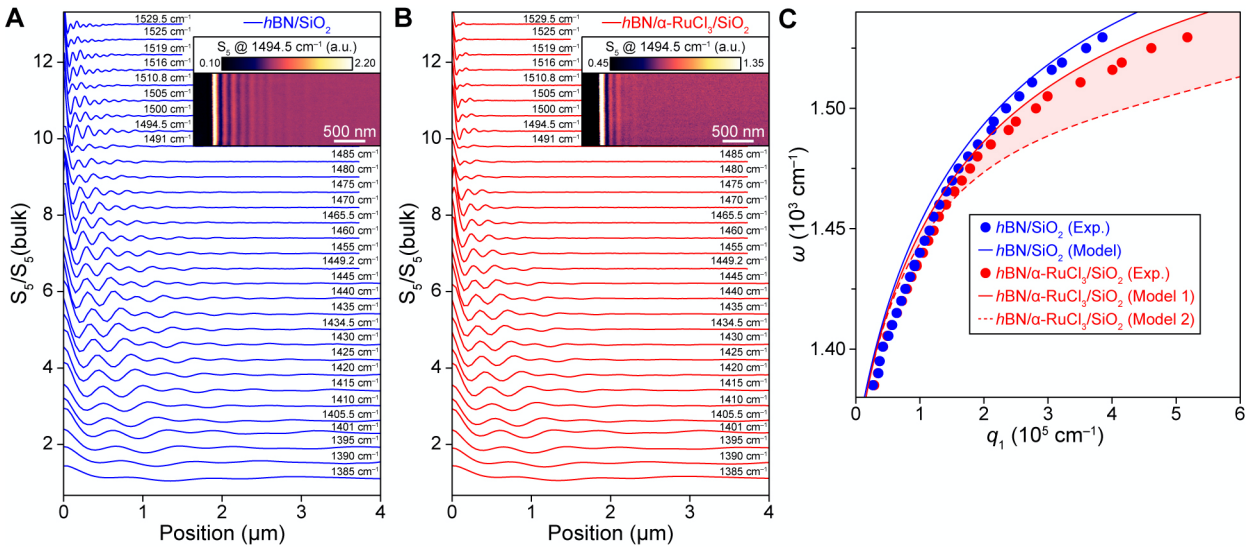

Figure S2. Frequency-dependent line profiles of PhP fringes. (**A**) Area-averaged line profiles of the near-field amplitude for *h*BN/SiO_2 showing PhP fringes collected at the indicated frequencies. A 0.4 offset is added between consecutive curves for clarity. The PhP wavelength clearly disperses with frequency. (**B**) The same as (A) but for PhPs propagating in *h*BN/α-$RuCl_3$/SiO_2. Each curve in (A) and (B) was truncated at the first minimum next to the *h*BN edge, and fit to the ansatz from refs. 1,2 to extract the complex wavevector $\boldsymbol{q}$. The ansatz is $S_0 + A\frac{e^{-iqx}}{R^a+x^a} + BH_0^{(1)}(2\boldsymbol{q}x)$, where S_0 is the bulk near-field amplitude, R is the approximate tip radius (25 nm), $H_0^{(1)}$ is the first Hankel function of order zero, A and B are sample angle- and tip-dependent scaling factors, respectively, and a is a geometric factor ≈0.1. (**C**) The experimentally extracted PhP dispersion for *h*BN on bare SiO_2 (solid blue circles) and on a layer of α-$RuCl_3$ (solid red circles). The expected PhP dispersions (i.e., maxima in $Im[r_p]$) for both regions are plotted with solid blue and solid red lines, respectively. The dashed red line shows the expected PhP dispersion when α-$RuCl_3$ is modelled with emergent interfacial losses (Model 2 in Fig. 3 of the main text), with the shaded red region highlighting the change in the dispersion.

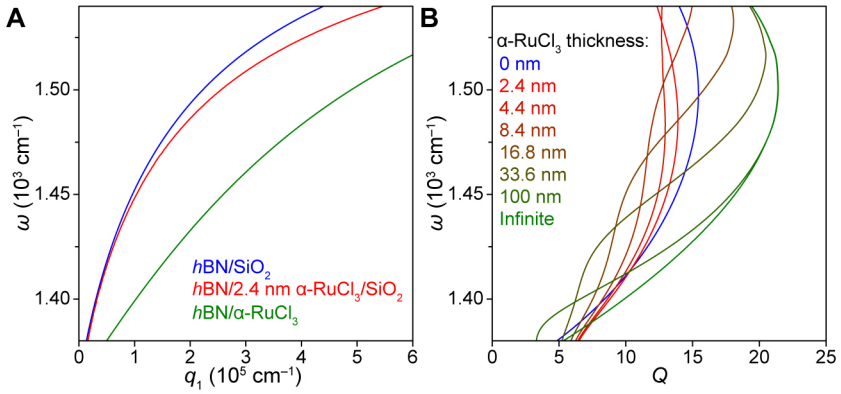

Figure S3. Model *h*BN PhP dispersion and *Q* for different thickness of α-$RuCl_3$. (**A**) The model dispersion for PhPs propagating in a 22-nm-thick *h*BN crystal on a thick slab of SiO_2 (blue curve), on a 2.4-nm-thick flake of α-$RuCl_3$ on a thick slab of SiO_2 (red curve), and on a thick slab of α-$RuCl_3$ (green curve). The dispersion is derived from maxima in the imaginary component of the *p*-polarized reflection coefficient, $Im[r_p]$. The *h*BN PhPs become more confined with thicker layers of underlying α-$RuCl_3$. (**B**) The frequency-dependent *Q* factor for PhPs propagating in a 22-nm-thick *h*BN crystal on a thick slab of SiO_2 (blue curve), on a 2.4-nm-thick flake of α-$RuCl_3$ on a thick slab of SiO_2 (red curve), and on a thick slab of α-$RuCl_3$ (green curve). The frequency-dependent *Q* is plotted for several intermediate thicknesses of α-$RuCl_3$ as indicated by the colored labels. While stacks with thinner α-$RuCl_3$ show a marginally lower value of *Q* compared to those directly on SiO_2, those with thicker α-$RuCl_3$ eventually show larger values of *Q*. The *Q* factor is calculated as outlined in the methods and supplementary discussion.

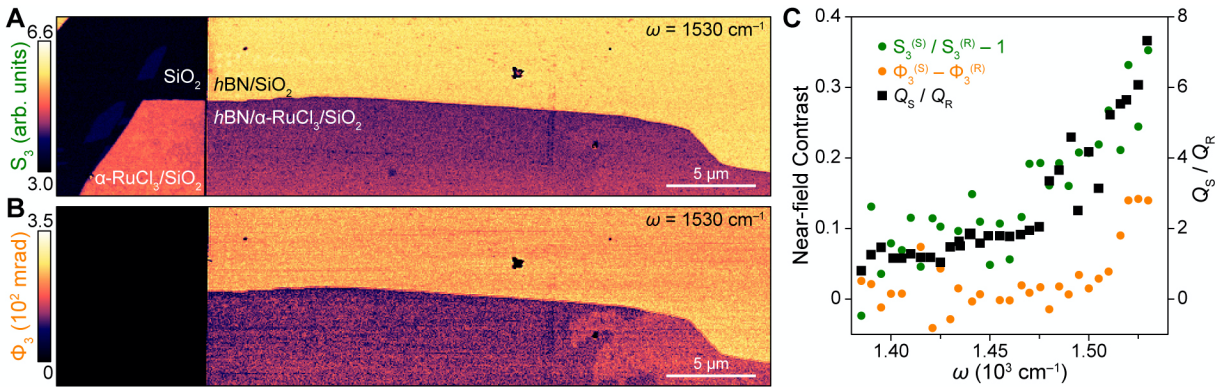

Figure S4. Near-field spectroscopy of *h*BN/α-RuCl$_3$ heterostructures. (**A**) Near-field S_3 amplitude at $\omega = 1530$ cm^{-1} of a heterostructure with *h*BN/α-RuCl$_3$/SiO$_2$, *h*BN/SiO$_2$, α-RuCl$_3$/SiO$_2$, and SiO$_2$ regions labelled. (**B**) The corresponding Φ_3 phase simultaneously collected in the same region as (A). (**C**) Plot of the frequency-dependence of the near-field contrast (solid green and orange circles are $S_3^{(S)} / S_3^{(R)} - 1$and $\Phi_3^{(S)} - \Phi_3^{(R)}$, respectively) and the ratio Q_S / Q_R (solid black squares). Here, $S_3^{(S)}$ and $S_3^{(R)}$ are the S_3 amplitudes averaged on *h*BN/SiO$_2$ and *h*BN/α-RuCl$_3$/SiO$_2$, respectively, and $\Phi_3^{(S)}$ and $\Phi_3^{(R)}$ are the Φ_3 phases averaged on *h*BN/SiO$_2$ and *h*BN/α-RuCl$_3$/SiO$_2$, respectively. The ratio between PhP *Q*-factors off and on α-RuCl$_3$ (Q_S / Q_R) increases with frequency in a manner that scales similarly to the near-field contrast.

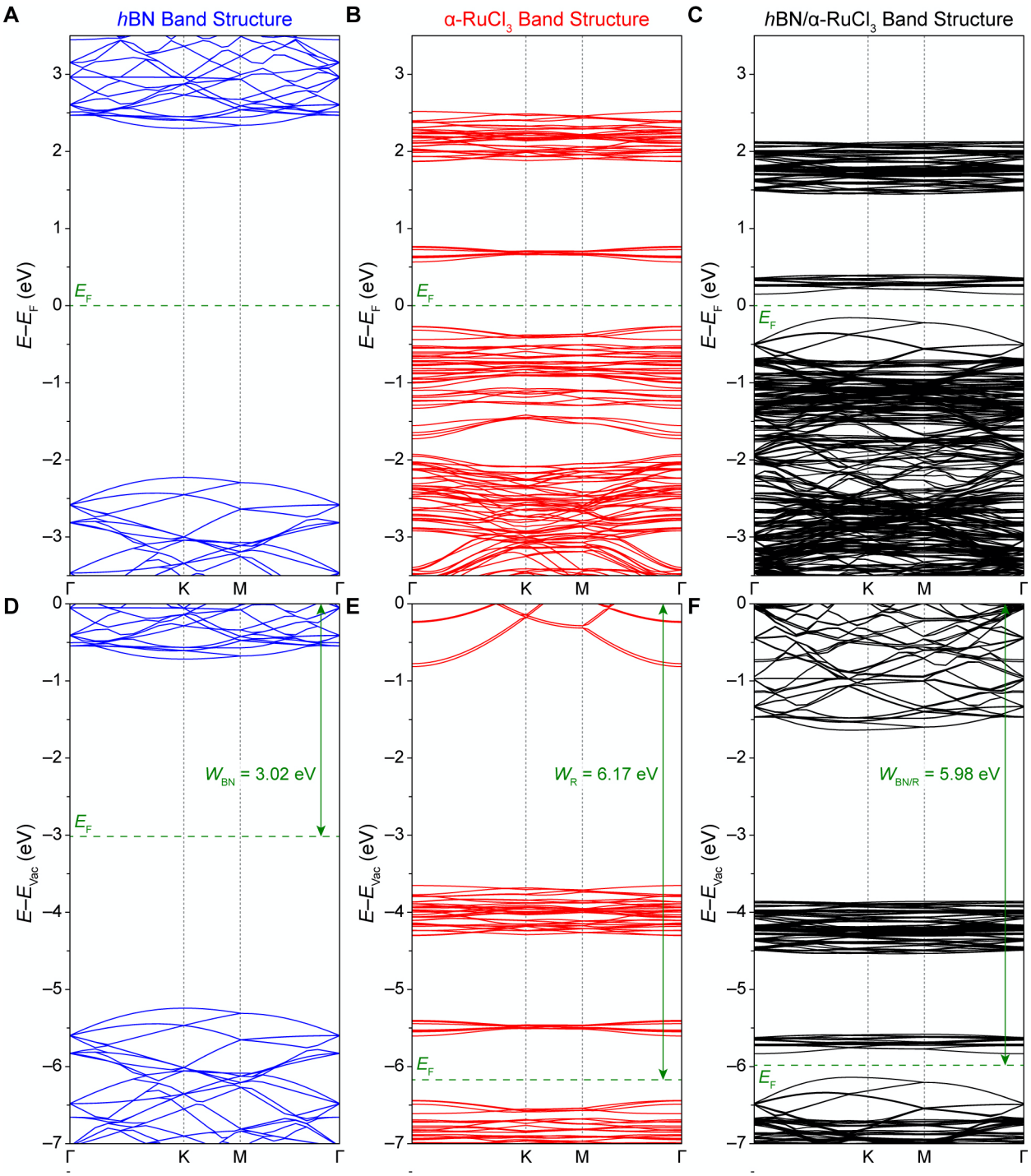

Figure S5. Comparison of band structures for free-standing and heterostructured *h*BN and α-$RuCl_3$. (**A**) Fermi energy-aligned free-standing band structures for monolayer *h*BN, (**B**) monolayer α-$RuCl_3$, and (**C**) monolayer-on-monolayer *h*BN/α-$RuCl_3$. (**D**-**E**) The same band structures plotted in (**A**-**C**) aligned relative to the vacuum energy. In their free-standing states, the *h*BN valence band (VB) is aligned energetically with the α-$RuCl_3$ conduction band (CB). The work function difference leads to the formation of an interfacial dipole in *h*BN/α-$RuCl_3$ that induces a small energy gap between the *h*BN VB and the α-$RuCl_3$ CB when heterostructured.

Supplementary Methods

Material Growth

α-$RuCl_3$ crystals were grown by the sublimation of $RuCl_3$ powder sealed in a quartz tube under vacuum. About 1 g of powder was loaded in a quartz tube of 19 mm in outer diameter, 1.5 mm thick, and 10 cm long. The growth was performed in a box furnace. After dwelling at 1060 °C for 6 h, the furnace was cooled to 800 °C at a rate of 4 °C/h. Magnetic and specific heat measurements confirmed that the as-grown pristine crystal orders antiferromagnetically around 7 K. For more information, see ref. 3.

Device Fabrication

The *h*BN/α-$RuCl_3$ heterostructures were assembled using standard dry-stacking with the hot pick-up method.[4,5] Specifically, we use a polycarbonate (PC) film on a polydimethylsiloxane (PDMS) stamp to pick up *h*BN exfoliated on a SiO_2/Si substrate at a temperature of 90 ºC. The *h*BN is then brought in contact with the target α-$RuCl_3$ crystal, also on SiO_2/Si, at a temperature of ~150 ºC. By using a higher temperature and a slow contact approach (~1 μm/min), we are able to push out most interfacial contamination, leaving us with a clean *h*BN/α-$RuCl_3$ interface. Finally, the PC film is dissolved in chloroform.

Scanning Near-field Optical Microscopy:

The s-SNOM measurements in this study were conducted using a commercial Neaspec system under ambient conditions using commercial Arrow^{TM} AFM probes with a nominal resonant frequency of f = 75 kHz. Tunable continuous wave quantum cascade lasers produced by Daylight Solutions were used spanning wavelengths from 6 to 8 μm. The detected signal was demodulated at the fourth or fifth harmonic of the tip tapping frequency in order to reduce background far-field contributions to the scattered light. The n^{th} harmonic of the near-field scattering amplitude (S_n) and phase (Φ_n) were collected simultaneously using a pseudoheterodyne interferometry technique.

Ab-initio Calculations of *h*BN/α-$RuCl_3$ Heterostructures:

The ab initio calculations were performed within the Vienna Ab initio Simulation Package (VASP)[6] using a projector-augmented wave (PAW) pseudopotential in conjunction with the Perdew–Burke–Ernzerhof (PBE)[7] functionals and plane-wave basis set with energy cutoff at 400 eV. For the heterostructures formed by *h*BN on top of a monolayer of α-$RuCl_3$, we used a fixed hexagonal supercell containing 170 atoms (composed of 3 x 3 α-$RuCl_3$ and 7 x 7 *h*BN). The resulting strain imposed on the heterostructure is ~2.1%. This strain doesn't modify the formation of the large interfacial dipole discussed in the present work. The surface Brillouin zone was sampled by a 3 × 3 × 1 Monkhorst–Pack k-mesh. A vacuum region of 15 Å was applied to avoid artificial interaction between the periodic images along the z direction. Due to the absence of strong chemical bonding between layers, we incorporate van der Waals interactions for structural optimization via the opt88 density functional introduced in ref. 8. All heterostructures for the above supercell size were fully relaxed until the force on each atom was less than 0.01 eV $Å^{-1}$. Spin-orbital couplings are included in the electronic calculations.
As shown in previous work (ref. 1) standard DFT functionals do not cope with the electronic structure of α-$RuCl_3$ as it requires accounting for on-site correlations via a Hubbard U for Ru and Cl atoms. The Hubbard U terms are computed by employing the generalized Kohn–Sham

equations within density functional theory including mean-field interactions, as provided by the Octopus package,[9,10] using the ACBN0[11,12] functional together with the local density approximation (LDA) functional describing the DFT part. We compute ab initio the Hubbard U and Hund's J for the 4d orbitals of Ruthenium and 3p orbital of Chlorine. We employ norm-conserving HGH pseudopotentials to get converged effective Hubbard U values of 1.96 eV for Ru 4d orbitals and 5.31 eV for Cl 3p orbitals, with spin-orbital couplings.

Supplementary Discussion

Calculating polariton dispersions and quality factors

Polariton dispersions $q_1(\omega)$ and quality factors $Q(\omega)$ in the main text are computed from the poles of the p-polarized reflection coefficient r_p. A condition for poles of r_p in a single finite *h*BN slab geometry corresponding to the fundamental polariton mode dispersion can be written in the following form:

$$2k_z d + \delta_{sub} + \delta_{sup} = 0$$

where $e^{i\delta_j} \approx \frac{1-i\frac{\varepsilon_j}{\sqrt{-\varepsilon_\parallel \varepsilon_z}}}{1+i\frac{\varepsilon_j}{\sqrt{-\varepsilon_\parallel \varepsilon_z}}}$ and $k_z \approx \sqrt{-\frac{\varepsilon_\parallel}{\varepsilon_\perp} q^2}$ in the near-field limit.[13] $\varepsilon_\parallel$ and $\varepsilon_\perp$ are the in- and out-of-plane dielectric functions of *h*BN, respectively,[14] and $q(\omega) = q_1(\omega) + iq_2(\omega)$ is the in-plane momentum of light. $\varepsilon_{\text{sup}} = 1$ and ε_{sub} is the dielectric function of the substrate.

For two slabs (e.g., *h*BN/α-$RuCl_3$/SiO_2 model), we solve an equivalent problem numerically. We first compute the 2x2 transfer matrix M for the system and note that $r_p = M_{21}/M_{11}$. The formalism in Reference 15 was used to compute the transfer matrix. *Nota bene*: in the case of uniaxial media like *h*BN, one should use $\varepsilon_\parallel$ (not ε_z) in Equation 10 of Reference 15. One should also ensure that the proper branches of k_z in all slabs are used such that Im $k_z \geq 0$.[16] The complex in-plane propagation constant $q(\omega)$ is obtained from minimizing $|M_{11}|$ using scipy.optimize methods. We verified that the real part $q_1(\omega)$ corresponds to the maxima of Im $r_p(q, \omega)$ and the residual $|M_{11}|^2 \sim 10^{-7}$ for all ω. Finally, we compute $Q(\omega) \equiv \frac{q_1(\omega)}{q_2(\omega)}$.
Dielectric functions of SiO_2 and α-$RuCl_3$ (assuming isotropic) are obtained from References 17 and 18, respectively.

Nano-infrared point spectra of *h*BN/SiO_2 normalized to *h*BN/α-$RuCl_3$/SiO_2 were fit by optimizing the parameters of a Lorentzian oscillator dielectric function for α-$RuCl_3$ within the lightning rod model[19] framework:

$$\varepsilon = \varepsilon_\infty + \frac{f^2}{\omega_0^2 - \omega^2 - i\gamma\omega}$$

The best-fit oscillator strength, resonance frequency, scattering rate, and background permittivity were $f = 1992\ \text{cm}^{-1}$, $\omega_0 = 1543\ \text{cm}^{-1}$, $\gamma = 30.5\ \text{cm}^{-1}$, and $\varepsilon_\infty = 2.01$, respectively. These parameters were used to compute another set of complex $q(\omega)$ that we compared with the dispersions and quality factors obtained when using the bare α-$RuCl_3$ dielectric function extracted from far-field spectroscopy in Reference 18. We note that these oscillator parameters differ significantly from those associated with nearby phonons in *h*BN or electronic transitions in α-$RuCl_3$, suggesting that this phenomenological Lorentzian oscillator cannot be trivially reproduced through rigid shifts and/or broadening of the intrinsic optical spectrum of either heterostructure constituent.

References

[1] Rizzo, D. J., Jessen, B. S., Sun, Z., Ruta, F. L., Zhang, J., Yan, J.-Q., Xian, L., McLeod, A. S., Berkowitz, M. E., Watanabe, K., Taniguchi, T., Nagler, S. E., Mandrus, D. G., Rubio, A., Fogler, M. M., Millis, A. J., Hone, J. C., Dean, C. R. & Basov, D. N. Charge-Transfer Plasmon Polaritons at Graphene/α-$RuCl_3$ Interfaces. *Nano Lett.* **20**, 8438-8445, (2020).

[2] Woessner, A., Lundeberg, M. B., Gao, Y., Principi, A., Alonso-González, P., Carrega, M., Watanabe, K., Taniguchi, T., Vignale, G., Polini, M., Hone, J., Hillenbrand, R. & Koppens, F. H. L. Highly Confined Low-Loss Plasmons in Graphene–Boron Nitride Heterostructures. *Nat. Mater.* **14**, 421-425, (2015).

[3] May, A. F., Yan, J. & McGuire, M. A. A Practical Guide for Crystal Growth of Van Der Waals Layered Materials. *J. Appl. Phys.* **128**, 051101, (2020).

[4] Pizzocchero, F., Gammelgaard, L., Jessen, B. S., Caridad, J. M., Wang, L., Hone, J., Bøggild, P. & Booth, T. J. The Hot Pick-up Technique for Batch Assembly of Van Der Waals Heterostructures. *Nat. Commun.* **7**, 11894, (2016).

[5] Purdie, D. G., Pugno, N. M., Taniguchi, T., Watanabe, K., Ferrari, A. C. & Lombardo, A. Cleaning Interfaces in Layered Materials Heterostructures. *Nat. Commun.* **9**, 5387, (2018).

[6] Kresse, G. & Furthmüller, J. Efficient Iterative Schemes for Ab Initio Total-Energy Calculations Using a Plane-Wave Basis Set. *Phys. Rev. B* **54**, 11169-11186, (1996).

[7] Perdew, J. P., Burke, K. & Ernzerhof, M. Generalized Gradient Approximation Made Simple. *Phys. Rev. Lett.* **77**, 3865-3868, (1996).

[8] Klimeš, J., Bowler, D. R. & Michaelides, A. Van Der Waals Density Functionals Applied to Solids. *Phys. Rev. B* **83**, 195131, (2011).

[9] Andrade, X., Strubbe, D., De Giovannini, U., Larsen, A. H., Oliveira, M. J. T., Alberdi-Rodriguez, J., Varas, A., Theophilou, I., Helbig, N., Verstraete, M. J., Stella, L., Nogueira, F., Aspuru-Guzik, A., Castro, A., Marques, M. A. L. & Rubio, A. Real-Space Grids and the Octopus Code as Tools for the Development of New Simulation Approaches for Electronic Systems. *Physical Chemistry Chemical Physics* **17**, 31371-31396, (2015).

[10] Tancogne-Dejean, N., Oliveira, M. J. T., Andrade, X., Appel, H., Borca, C. H., Le Breton, G., Buchholz, F., Castro, A., Corni, S., Correa, A. A., De Giovannini, U., Delgado, A., Eich, F. G., Flick, J., Gil, G., Gomez, A., Helbig, N., Hübener, H., Jestädt, R., Jornet-Somoza, J., Larsen, A. H., Lebedeva, I. V., Lüders, M., Marques, M. A. L., Ohlmann, S. T., Pipolo, S., Rampp, M., Rozzi, C. A., Strubbe, D. A., Sato, S. A., Schäfer, C., Theophilou, I., Welden, A. & Rubio, A. Octopus, a Computational Framework for Exploring Light-Driven Phenomena and Quantum Dynamics in Extended and Finite Systems. *The Journal of Chemical Physics* **152**, 124119, (2020).

[11] Tancogne-Dejean, N., Oliveira, M. J. T. & Rubio, A. Self-Consistent *DFT+U* Method for Real-Space Time-Dependent Density Functional Theory Calculations. *Phys. Rev. B* **96**, 245133, (2017).

[12] Agapito, L. A., Curtarolo, S. & Buongiorno Nardelli, M. Reformulation of *DFT+U* as a Pseudohybrid Hubbard Density Functional for Accelerated Materials Discovery. *Physical Review X* **5**, 011006, (2015).

[13] Sun, Z., Gutiérrez-Rubio, Á., Basov, D. N. & Fogler, M. M. Hamiltonian Optics of Hyperbolic Polaritons in Nanogranules. *Nano Lett.* **15**, 4455-4460, (2015).
[14] Caldwell, J. D., Kretinin, A. V., Chen, Y., Giannini, V., Fogler, M. M., Francescato, Y., Ellis, C. T., Tischler, J. G., Woods, C. R., Giles, A. J., Hong, M., Watanabe, K., Taniguchi, T., Maier, S. A. & Novoselov, K. S. Sub-Diffractional Volume-Confined Polaritons in the Natural Hyperbolic Material Hexagonal Boron Nitride. *Nat. Commun.* **5**, 5221, (2014).
[15] Zhan, T., Shi, X., Dai, Y., Liu, X. & Zi, J. Transfer Matrix Method for Optics in Graphene Layers. *J. Phys.: Condens. Matter* **25**, 215301, (2013).
[16] Dai, S., Ma, Q., Liu, M. K., Andersen, T., Fei, Z., Goldflam, M. D., Wagner, M., Watanabe, K., Taniguchi, T., Thiemens, M., Keilmann, F., Janssen, G. C. A. M., Zhu, S. E., Jarillo-Herrero, P., Fogler, M. M. & Basov, D. N. Graphene on Hexagonal Boron Nitride as a Tunable Hyperbolic Metamaterial. *Nat. Nanotechnol.* **10**, 682-686, (2015).
[17] Fei, Z., Andreev, G. O., Bao, W., Zhang, L. M., McLeod, A. S., Wang, C., Stewart, M. K., Zhao, Z., Dominguez, G., Thiemens, M., Fogler, M. M., Tauber, M. J., Castro-Neto, A. H., Lau, C. N., Keilmann, F. & Basov, D. N. Infrared Nanoscopy of Dirac Plasmons at the Graphene–SiO_2 Interface. *Nano Lett.* **11**, 4701-4705, (2011).
[18] Reschke, S., Mayr, F., Widmann, S., von Nidda, H.-A. K., Tsurkan, V., Eremin, M. V., Do, S.-H., Choi, K.-Y., Wang, Z. & Loidl, A. Sub-Gap Optical Response in the Kitaev Spin-Liquid Candidate α-$RuCl_3$. *J. Phys.: Condens. Matter* **30**, 475604, (2018).
[19] McLeod, A. S., Kelly, P., Goldflam, M. D., Gainsforth, Z., Westphal, A. J., Dominguez, G., Thiemens, M. H., Fogler, M. M. & Basov, D. N. Model for Quantitative Tip-Enhanced Spectroscopy and the Extraction of Nanoscale-Resolved Optical Constants. *Phys. Rev. B* **90**, 085136, (2014).